Direct Imaging of Chiral Domain Walls and Néel-Type Skyrmionium in Ferrimagnetic Alloys

Boris Seng,* Daniel Schönke, Javier Yeste, Robert M. Reeve, Nico Kerber, Daniel Lacour, Jean-Loïs Bello, Nicolas Bergeard, Fabian Kammerbauer, Mona Bhukta, Tom Ferté, Christine Boeglin, Florin Radu, Radu Abrudan, Torsten Kachel, Stéphane Mangin, Michel Hehn, and Mathias Kläui*

The evolution of chiral spin structures is studied in ferrimagnetic Ta/Ir/Fe/GdFeCo/Pt multilayers as a function of temperature using scanning electron microscopy with polarization analysis (SEMPA). The GdFeCo ferrimagnet exhibits pure right-handed Néel-type domain wall (DW) spin textures over a large temperature range. This indicates the presence of a negative Dzyaloshinskii–Moriya interaction that can originate from both the top Fe/Pt and the Co/Pt interfaces. From measurements of the DW width, as well as complementary magnetic characterization, the exchange stiffness as a function of temperature is ascertained. The exchange stiffness is surprisingly more or less constant, which is explained by theoretical predictions. Beyond single skyrmions, it is identified by direct imaging a pure Néel-type skyrmionium, which due to the expected vanishing skyrmion Hall angle, is a promising topological spin structure to enable applications by next generation of spintronic devices.

1. Introduction

The competition between different interactions in magnetic materials leads to a wide variety of different magnetic spin structures from single-domain states to chiral spin textures. Among them, magnetic skyrmions in thin-film multilayer systems[1–7] are nowadays widely studied due to their attractive properties for potential applications including their room temperature (RT) stability.[1,8–10] Skyrmions are topological spin structures

that can be stabilized through an antisymmetric exchange interaction that arises in a system with a broken inversion symmetry: the Dzyaloshinskii–Moriya interaction (DMI).[11,12] Recent studies confirmed the current-driven dynamics of skyrmions in ultrathin ferromagnets via spin–orbit torques (SOTs) that act efficiently on Néel-type spin textures.[1,8,13] For deterministic dynamics, sufficient DMI is then required to yield homochiral domain walls (DW). Therefore, skyrmions stabilized with DMI are particularly suitable for next generation spintronics devices, such as the skyrmion-based racetrack memory.[8] However, the dynamics of ferrimagnetic skyrmions via SOTs exhibits a transverse motion due to their nonzero topological charge.[14–16] This behavior is especially unwanted in many applications since skyrmions could be annihilated at an edge of a device with the information carried by the skyrmion lost as a result. In ferrimagnets, the effective topological charge depends on the degree of compensation and can go effectively to zero at the compensation temperature. Therefore, materials with antiferromagnetically exchange-coupled magnetic sublattices have been proposed to reduce or annihilate this skyrmion Hall effect owing to a reduced effective topological charge.[17,18]

B. Seng, Dr. D. Schönke, J. Yeste, Dr. R. M. Reeve, N. Kerber,
F. Kammerbauer, M. Bhukta, Prof. M. Kläui
Institut für Physik
Johannes Gutenberg-Universität Mainz
Staudingerweg 7, 55128 Mainz, Germany
E-mail: boriseng@uni-mainz.de; klaeui@uni-mainz.de

B. Seng, Dr. D. Lacour, J.-L. Bello, Prof. S. Mangin, Prof. M. Hehn
Institut Jean Lamour
UMR CNRS 7198
Université de Lorraine
2 allée André Guinier, Nancy 54011, France

B. Seng, Dr. R. M. Reeve, N. Kerber, Prof. M. Kläui
Graduate School of Excellence Materials Science in Mainz
Staudingerweg 9, 55128 Mainz, Germany

B. Seng, N. Kerber, Prof. M. Kläui
Max Planck Graduate Center mit der Johannes Gutenberg-Universität
Staudingerweg 9, 55128 Mainz, Germany

Dr. N. Bergeard, T. Ferté, Dr. C. Boeglin
Université de Strasbourg
CNRS
Institut de Physique et Chimie des Matériaux de Strasbourg
UMR 7504, Strasbourg F-67000, France

Dr. F. Radu, Dr. R. Abrudan, Dr. T. Kachel
Helmholtz-Zentrum Berlin für Materialien und Energie
Albert-Einstein-Str. 15, 12489 Berlin, Germany

Ferrimagnetic materials such as rare earth (RE)—transition metal (TM) alloys are made of two antiferromagnetically exchange-coupled magnetic sublattices. For a given stoichiometry, at a temperature called the magnetization compensation temperature, the magnetization of the two sublattices is equal and opposite and therefore the net magnetization is zero.[19] Similarly, an angular momentum compensation temperature can be defined where a vanishing skyrmion Hall angle is predicted.[20] GdFeCo ferrimagnetic alloys have attracted significant attention since the discovery of all-optical switching (AOS) in these alloys.[21] Since then two types of AOS have been observed[22,23] and the possibility to reverse the magnetization with a single electron pulse has been demonstrated.[24] In particular, to use these systems for devices based on topological spin structure, one needs deterministic behavior in devices and for that it is necessary that the DMI is sufficient to generate a single chirality of skyrmions with a Néel-type spin texture. This then enables efficient SOT driven DW or skyrmion motion. To realize this, one requires a detailed analysis and high resolution magnetic imaging of the internal spin structures of such ferrimagnetic skyrmions, which is still missing to date. In particular, as ferrimagnets can exhibit a strong temperature dependence of their properties, one needs to ascertain the temperature range where robust properties are found as, for instance, the skyrmion Hall angle and the thermal dynamics depend on the topological charge of the system.[25]

In this study, we investigate the chirality of spin textures in a ferrimagnet, namely Ta/Ir/Fe/GdFeCo/Pt, by imaging the spin structure of the DW using scanning electron microscopy with polarization analysis (SEMPA).[26–28] This surface-sensitive imaging technique has already been successfully used to determine the chiral character of out-of-plane (OOP) magnetized spin textures in ferromagnetic materials[29,30] and here we demonstrate that we can determine the chiral character of spin textures also for ferrimagnetic materials. From the SEMPA images, we are also able to extract the DW width across a wide range of temperatures, which allows us to determine the exchange stiffness evolution with temperature as a crucial parameter that governs the stability and operation temperature range.

2. Results and Discussion

The Ta/Ir/Fe/GdFeCo/Pt sample (details see section 4) exhibits perpendicular magnetic anisotropy with a small switching field after milling (see the Supporting Information S6). The stabilization of spin textures is achieved by cycling an in-plane (IP) magnetic field at RT where structures start to nucleate randomly. **Figure 1**a,b shows the direction and the magnitude of the in-plane magnetization, respectively M_x and M_y, imaged with SEMPA under zero magnetic field after the nucleation process.
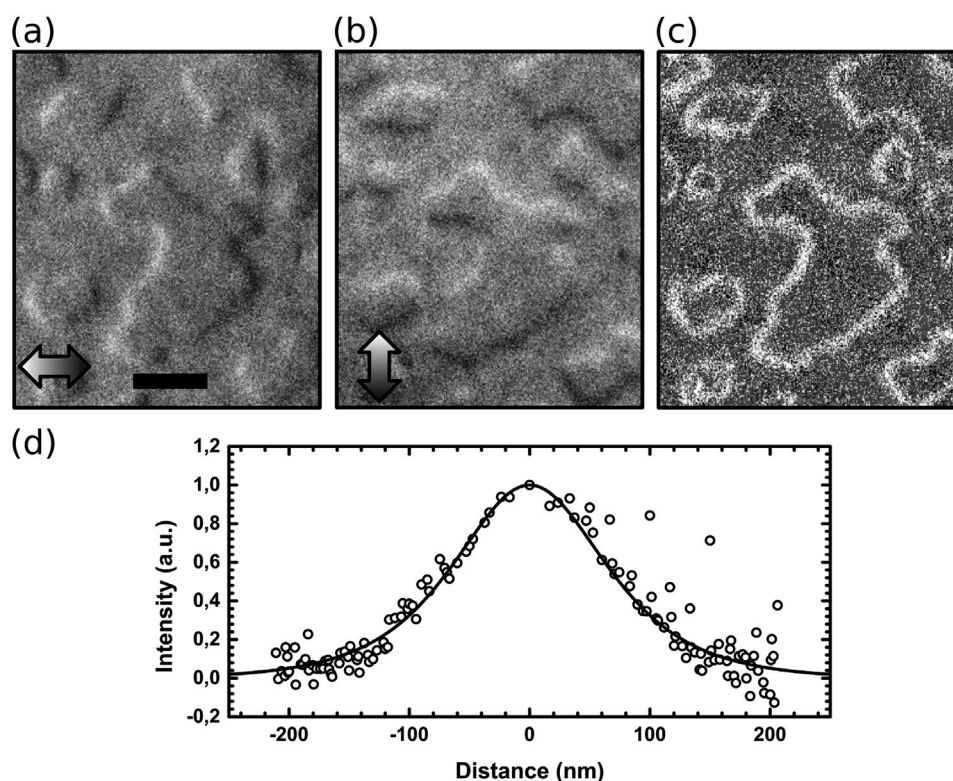

Figure 1. Determination of the average DW width of spin textures in Ta/Ir/Fe/GdFeCo/Pt taken with SEMPA at RT. a) Horizontal and b) vertical in-plane components of the magnetization. The direction of magnetization is indicated by the grayscale contrast, as displayed on the double arrows. Scale bar in a): 1 μm. c) Reconstruction of the absolute in-plane magnetization intensity. The white contrast indicates a saturated in-plane magnetization. d) Distribution of the average DW intensity profile for all the spin textures present in the image (unfilled circles) and a fit to Equation (1) (black line). The zero position represents the center of the skeleton.

Contrast in the DW can be observed, where the in-plane magnetization is expected, with a brighter contrast present for the left (top) of each domain indicating a left (up) tendency for the local direction of the magnetization. Conversely, dark contrast is seen at the right (bottom) edges of the domains, as shown in Figure 1a,b. In Figure 1c, the absolute in-plane magnetization image has been generated using $|\overline{M}|_{IP} = \sqrt{M_x^2 + M_y^2}$ at each local position of the image where the brighter contrast indicates the in-plane saturated magnetization. This contrast clearly indicates the position of the DW where in-plane components are then present. From the analysis, the position of the skeleton of the DW, i.e., the line at the center of the DW, can then be defined. The determination of the skeleton allows us to establish the DW intensity profile shown in Figure 1d by averaging the measured local DW profile at each position of the skeleton (see the Supporting Information S7). However, the imaged DW profile needs to be carefully analyzed in order to obtain the true profile, principally due to the broadening of the features due to the finite size of the beam profile. The experimental profile can be approximated as the convolution of the theoretical DW profile with a Gaussian function (describing the electron beam distribution) as follows

$$DW_{profile} \propto \cosh^{-1}\left(\frac{x}{\Delta}\right) \otimes e^{-\frac{x^2}{2\sigma^2}} \qquad (1)$$

where the hyperbolic function represents the real DW profile with Δ the Bloch parameter. In our case, we use for the DW width δ, defined by Lilley where $\delta = \pi\Delta$.[31] To determine the Gaussian function, we consider a sharp defect modeled as a step function

(see the Supporting Information S5). The Gaussian is found to be narrower than the imaged DW and here it has a rather small but non-negligible influence on the DW width measurements. From this analysis, we finally determine the real DW width to be $\delta_{real} = 175 \pm 5$ nm at RT.

After having defined the DW width, we analyze the spin distribution within the DW. For that, we extract the magnitude and the direction of the in-plane magnetization M_x and M_y at each position of the DW displayed in Figure 1a,b and we deduce geometrically the angle that corresponds to the direction of the in-plane magnetization inside the wall. **Figure 2**a displays the direction of the in-plane magnetization in the DW by way of the color wheel shown in the inset. Qualitatively, we first see that all the magnetic structures present the same chirality, namely they are homochiral clockwise Néel-type spin textures. For a precise analysis, we then compare the spin direction of each position inside the DW with the direction of the local tangent of the DW (Figure 2b) (see the Supporting Information S7). The histogram indicates that the magnetization direction in the DW structures forms a distribution centered around −90°. We conclude that our material exhibits a pure clockwise Néel-type homochiral character, which can be explained by the negative sign of the interfacial DMI at typical Fe/Pt and Co/Pt interfaces when the Pt layer is on top of the Fe or Co layer. Since SEMPA is a surface sensitive technique, we only probe the direction of the magnetization close to the surface. To ascertain that this chiral character is not a local effect at the surface due to flux closure but is indeed supported through the whole thickness of the film, asymmetric bubble expansion has been performed that confirms our clockwise Néel homochirality in the full film.[32]
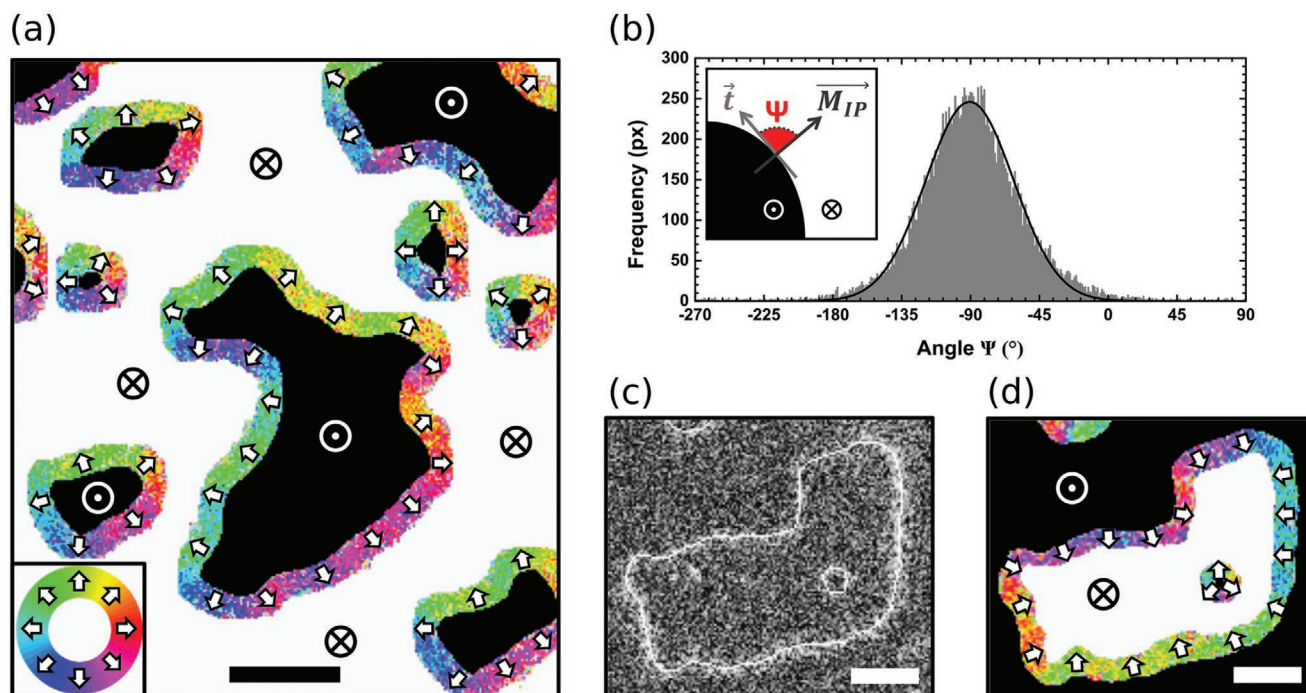

Figure 2. Determination of the magnetization direction inside the DW of different ferrimagnetic chiral spin textures. a) The direction of the in-plane magnetization in the DW is displayed, as defined by the color wheel in the bottom left corner of the image. Scale bar in a): 1 µm. b) Distribution of the direction of the in-plane magnetization $\overrightarrow{M_{IP}}$ in the DW with respect to the local tangent $\vec{t}$ at RT: angle Ψ (see inset where a clockwise angle is defined as negative following the usual convention). A Gaussian fit indicates a central value around −90°. c) Absolute in-plane magnetization intensity with the DW skeleton displayed in white and d) direction of the in-plane magnetization in the DW of a ferrimagnetic skyrmionium at 320 K. Scale bars in c,d): 500 nm.

As explained above, an IP magnetic field is used to nucleate spin textures that start to propagate at random positions. Remarkably, using an IP oscillating magnetic field with a certain damping ratio allows for the nucleation of a spin texture inside another spin texture that has been nucleated previously. In Figure 2c,d, one can observe a small 160 nm diameter skyrmion stabilized in a larger skyrmion bubble, forming a magnetic skyrmionium.[33,34] We here apply the topology definition that identifies skyrmions from the topology of the spin structure independent of their size.[35] This topological spin texture is especially attractive due to its zero topological charge at all temperatures,[33–36] which should lead to a vanishing skyrmion Hall angle that is promising for application.

To extract the key magnetic parameters of the system, we analyze the measured DW profiles by considering the model put forward in I. Lemesh et al.[37] In that work, the authors demonstrated that the DW width Δ is given by

$$\Delta(d, \Psi) = \Delta_0 - \cfrac{1}{\cfrac{2\pi(Q-1)}{d} + \cfrac{1}{\Delta_0 - \Delta_\infty(\Psi)}} \quad (2)$$

where d is the thickness of the magnetic material and Ψ is the DW angle; $\Delta_0 = \sqrt{\dfrac{A}{K_{eff}}}$, $\Delta_\infty = \sqrt{\dfrac{A}{K_u + \dfrac{\mu_0 M_s^2}{2}\sin^2(\Psi)}}$,

$Q = \dfrac{2K_u}{\mu_0 M_s^2}$, $K_{eff} = K_u - \dfrac{\mu_0 M_s^2}{2}$ depending on the exchange stiffness A, the uniaxial anisotropy K_u, and the saturation magnetization M_s.

The DMI dependence of the DW width enters via the angle Ψ. In the case of pure-Néel type DW, above a certain DMI threshold value, the exact value of the DMI does not affect the DW width since $|\Psi| = 90°$. In this case, by measuring the saturation magnetization M_s and the effective anisotropy K_{eff} (defined as the difference in the areas of the IP and OOP hysteresis loops) using a Superconducting Quantum Interference Device (SQUID), the exchange stiffness can be evaluated from the DW profile to be $A = 8.0 \pm 0.5$ pJ m^{-1} at RT. Therefore, through the measurement of the DW width via SEMPA, it is possible to determine the exchange stiffness of a material, a parameter that is not easily accessible using other simple techniques.

One crucial point for the use of magnetic skyrmions in spintronic devices is the conservation of the homochiral character of the DW over a large temperature range. Since a stray field favors Bloch-type DW, the observation of pure Néel-type DW observed at RT where the saturation magnetization is high (see the Supporting Information S4) allows us to identify a strong DMI in the system. Therefore, we can expect to always stabilize pure Néel-type spin textures at all other temperatures where the saturation magnetization is even lower in this sample. To assess this, the previous analysis has been carried out from 26 to 315 K. We see in **Figure 3**a that the pure Néel character remains for this temperature range. Next, we analyze the DW width for these temperatures, with the different values reported in Figure 3b. We find that the DW are narrower when

the temperature is decreased due to the increase of the effective anisotropy that is confirmed by SQUID. The results can be analyzed with the help of measurements of the thermal variation of K_{eff} and M_s at different temperatures (Figure 3c). As expected for the CoFe transition metal dominant ferrimagnet, lower temperatures lead to a reduction in the saturation magnetization since the rare earth sublattice magnetization increases faster than the transition metal one. On the other
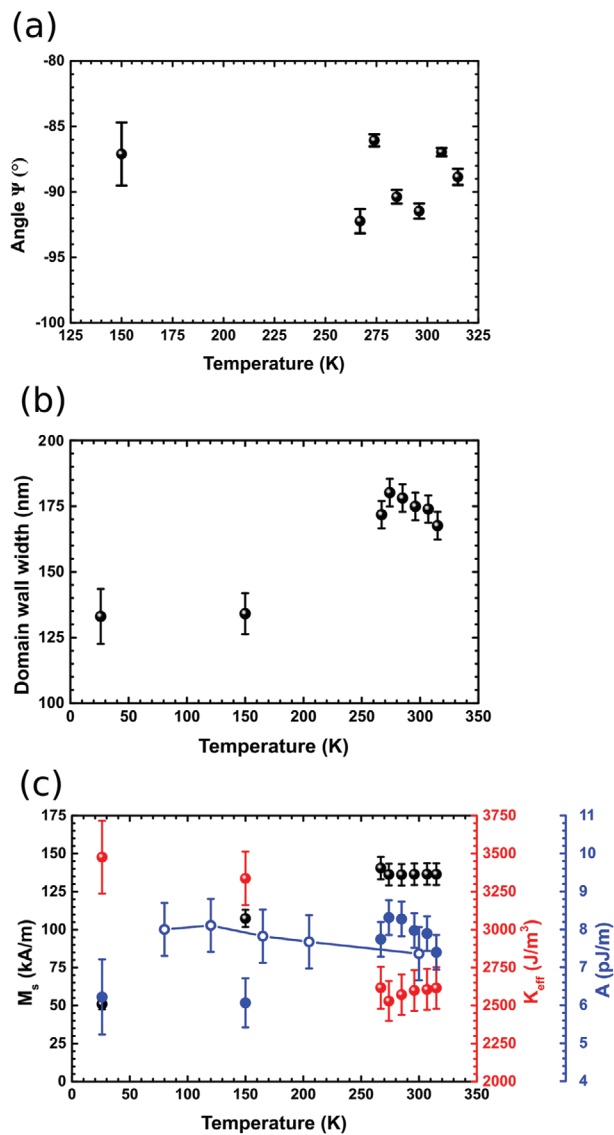

Figure 3. Measurements and determination of magnetic parameters of the ferrimagnetic multilayer. a) Average value of the magnetization angle within the DW, Ψ, at different temperatures for the TM dominant GdFeCo ferrimagnet. The angle of the magnetization inside the DW at 26 K could not be precisely determined due to the noise of the measurement, even though a pure Néel character was clearly present. b) DW width measurements as a function of temperature. c) Display of the exchange stiffness (blue) for different temperatures as well as the saturation magnetization M_s (black) and the effective anisotropy K_{eff} (red). Blue filled circles represent the exchange stiffness deduced from DW width measurements and magnetic characterization of our GdFeCo ferrimagnet based on Equation (2). Blue open circles represent the exchange stiffness deduced from XMCD measurements of $Co_{84}Gd_{16}(20)$ using Equation (3), for comparison.

hand, K_{eff} increases when the temperature decreases. Since the chiral character is kept over the whole temperature range and $|\Psi| = 90°$, Equation (2) can be used to extract the thermal variation of the exchange stiffness of the ferrimagnetic alloy over the whole temperature range. The exchange stiffness is found to be mostly constant, with a slight increase when the temperature increases, as shown in Figure 3c.

This dependence of the exchange stiffness on temperature is counterintuitive since in ferromagnetic materials, $A(T)/A(0)$ is expected to vary as $(M(T)/M(0))^{\gamma}$ with γ around 2.[38,39] Considering that in ferrimagnets the magnon spectrum consists of acoustic and optical branches, Nakamura et al. have shown that the temperature dependence of $A(T)$ is rather weak up to a certain high temperature.[40] This is due to the competing effects of thermal-acoustic and optical magnons. $A(T)$ then decreases when T decreases in the case of acoustic branch magnons. This prediction has been compared to experimental data by Srivastava et al. for YIG and magnetite and a satisfactory agreement have been obtained.[41] In their paper, they proposed a comprehensive description of the dependence via the relationship

$$\frac{A(T)}{A(0)} = \frac{\left(\dfrac{M_a(T)}{M_a(0)}\right)\left(\dfrac{M_b(T)}{M_b(0)}\right)}{(M_a(T) - M_b(T))(M_a(0) - M_b(0))} \quad (3)$$

where $M_a(T)$ and $M_b(T)$ are the thermal variation of the magnetization of the sublattices a and b, which we now want to use to analyze our data.

While very little experimental data on the variation of $A(T)$ for ferrimagnetic systems is available, and to our knowledge none on the GdFeCo system, we can use experimental data sets acquired by means of element selective X-ray magnetic circular dichroism (XMCD) spectroscopy (see the Supporting Information S8) on a 20 nm thick $Co_{84}Gd_{16}$ alloy to extract $M_{Co}(T)$ and $M_{Gd}(T)$ and then to derive $A(T)$ using Equation (3).[42] The compensation temperature of this alloy is the same as our 8 nm thick $Gd_{26.1}Fe_{65.5}Co_{8.3}$ alloy. The result of $A(T)$ is shown in Figure 3c. We find that $A(T)$ is roughly constant between 80 and 350 K, in line with the experimental data of our GdFeCo ferrimagnet. The good agreement allows us to conclude that the exchange stiffness does not vary strongly as a function of temperature, showing robust behaviors over the full temperature range.

3. Conclusion

In this study, we demonstrate imaging of the internal spin structure of domains and DW in GdFeCo ferrimagnetic alloys through a residual Pt capping layer using SEMPA. This approach is a new path to characterize chiral spin textures in ferrimagnetic multilayers. In the studied GdFeCo-based ferrimagnet, we find that the DW spin textures exhibit a pure Néel-type homochirality that is preserved over a large temperature range, even far away from the compensation temperature. This makes GdFeCo a potentially attractive material for skyrmion-based spintronic technologies. Our

corrected values of the DW width obtained from the high resolution imaging allow us then to extract the exchange stiffness in our material. We can explain the surprising temperature dependence of the exchange stiffness from a theoretical model taking into account the multiple magnetic sublattices in the material. Finally, in addition to chiral spin textures, we report the first direct observation of pure Néel-type skyrmionium in ferrimagnetic materials, which has the advantage of possessing zero net topological charge at all temperatures. This makes the material potentially highly useful for skyrmionic devices where the skyrmion Hall angle could be avoided.

4. Experimental Section

A multilayer thin film of $Si//Ta(5)/Ir(5)/Fe(0.3)/Gd_{26.1}Fe_{65.5}Co_{8.3}(8)/Pt(5)$ was deposited using magnetron sputtering in a chamber with a base pressure of 2.4×10^{-8} Torr, with the thickness of each individual layer given in nanometers in parentheses. The ferrimagnetic layer was grown by cosputtering and the atomic compositions were estimated from the deposition rates of each target. To ascertain the quality of the film, X-ray reflectivity (XRR) (see the Supporting Information S1) and atomic force microscopy (AFM) (see the Supporting Information S2) were performed that demonstrate a high degree of smoothness of the different interfaces and the surface.

The $Gd_{26.1}Fe_{65.5}Co_{8.3}(8)$ alloy was chosen for its low coercivity that makes the stabilization of OOP spin textures by magnetic fields easier. To demonstrate its amorphous nature, X-ray diffraction was performed (see the Supporting Information S3) with no undesirable crystallographic order detected for the GdFeCo. The CoFe dominant alloy phase was selected to provide a lower compensation temperature to avoid sample heating effects (see the Supporting Information S4). Interfacial DMI comes from a strong spin–orbit coupling with broken inversion symmetry between a heavy metal (HM) and ferromagnetic materials (FM) that arises mainly from the first atomic layer.[43] An ultrathin Fe(0.3) dusting layer was inserted between Ir and the ferrimagnetic layer to enhance the interfacial DMI, which was calculated to be negative at the Ir/Fe interface.[44] However, it was also noted that there are also estimates of a positive DMI at Ir/Fe interfaces.[43] Therefore, one has to be careful with assumptions concerning the sign of the interfacial DMI at the Ir interface. At the other interface, the DMI at the Co/Pt or Fe/Pt interfaces is expected to be strong and negative.[2,43,45]

To enable surface sensitive SEMPA imaging, Ar ion milling was performed to remove around 3.5 nm of the 5 nm Pt capping layer. In SEMPA, a primary beam of 3 nA at 7.5 keV was used to image the DW magnetization orientation via the spatially resolved detection of the spin-polarized secondary electrons from the magnetic layer. In the case of RE–TM ferrimagnets, the SEMPA acquisition was primarily sensitive to the magnetization of the TM sublattice which then allows to determine the system chirality even in the case of a reduced net magnetization of the RE–TM alloy near compensation. Since SEMPA is a very surface sensitive technique with a relatively low-efficiency of the spin-detection[46] and the imaging was performed through a residual Pt cap layer,[47] very long acquisition times were needed (about 20 h per image). The top Pt interface was only partially removed to retain a sizable negative DMI interaction at the top interface, as well as to retain an out-of-plane anisotropy, while still enabling the SEMPA imaging. To avoid a reduction in the image resolution as a result of thermally induced drift of the image during such long acquisitions, the field of view with a fast scan frequency of 1000 pixels s^{-1} resulting in a total dwell time of 1 ms per pixel was repeatedly scan. The secondary electrons emitted from the sample surface were collected by electron optics and were scattered on a W(001) crystal. As a result of spin-dependent low energy electron diffraction (LEED), they were preferentially scattered in different directions depending on their spin and then detected via single-electron

ADVANCED
SCIENCE NEWS

www.advancedsciencenews.com

ADVANCED
FUNCTIONAL
MATERIALS

www.afm-journal.de

counters. Calculating the normalized asymmetries of the electron flux at the opposite (2,0) LEED spots gave the x and y SEMPA asymmetry images that correspond to the in-plane magnetization components of the sample surface.[48] Before further analysis, a linear gradient correction was applied to the asymmetry images, which quantitatively reflect the x and y components of the magnetization vector, M_x and M_y. From these images, a third image of the absolute in-plane magnetization vector $\overline{M}_{IP}$ was calculated showing the position of the DW. Outside the DW, the measured absolute in-plane magnetization value was close to zero since the domains are oriented out of the plane. However, within the DW, a measurable in-plane component exists and was detected. The spatial resolution was determined by imaging the edge of a particle in the SEMPA topography image, where all four detector channels were added up. The spatial resolution was found to be equal to about 28 nm (see the Supporting Information S5).

Supporting Information

Supporting Information is available from the Wiley Online Library or from the author.

Conflict of Interest

The authors declare no conflict of interest.

Author Contributions

M.K., M.H., and S.M. proposed the study. M.K., M.H., S.M., and R.M.R. supervised the study. B.S, M.H., and J.-L.B grew the samples and B.S. and M.H. optimized the samples. D.S., R.M.R., B.S, J.Y., and M.B. performed the SEMPA imaging. B.S, D.S, J.Y., and D.L performed the analysis of the SEMPA images. B.S., F.K., and N.K. performed the magnetometry. F.K. and B.S. performed XRR and XRD. B.S and D.L performed AFM. F.R and R.A are the HZB's local contact that operated the ALICE reflectometer, while T.K. is in charge of the PM3 beamline at BESSY II. C.B, T.F., and N.B performed the XMCD measurements and took care of the analysis. B.S. drafted the manuscript with the help of M.K., M.H., R.M.R., S.M., and N.B. All the authors commented on the manuscript.

Data Availability Statement

The data that support the findings of this study are available from the corresponding author upon reasonable request.

[1] S. Woo, K. Litzius, B. Krüger, M.-Y. Im, L. Caretta, K. Richter, M. Mann, A. Krone, R. M. Reeve, M. Weigand, P. Agrawal, I. Lemesh, M.-A. Mawass, P. Fischer, M. Kläui, G. S. D. Beach, *Nat. Mater.* **2016**, *15*, 501.

[2] C. Moreau-Luchaire, C. Mouta S, N. Reyren, J. Sampaio, C. A. Vaz, N. Van Horne, K. Bouzehouane, K. Garcia, C. Deranlot, P. Warnicke, P. Wohlhüter, J.-M. George, M. Weigand, J. Raabe, V. Cros, A. Fert, *Nat. Nanotechnol.* **2016**, *11*, 444.

[3] O. Boulle, J. Vogel, H. Yang, S. Pizzini, D. de Souza Chaves, A. Locatelli, T. O. Menteş, A. Sala, L. D. Buda-Prejbeanu, O. Klein, M. Belmeguenai, Y. Roussigné, A. Stashkevich, S. M. Chérif, L. Aballe, M. Foerster, M. Chshiev, S. Auffret, I. M. Miron, G. Gaudin, *Nat. Nanotechnol.* **2016**, *11*, 449.

[4] B. W. Qiang, N. Togashi, S. Momose, T. Wada, T. Hajiri, M. Kuwahara, H. Asano, *Appl. Phys. Lett.* **2020**, *117*, 142401.

[5] W. Jiang, G. Chen, K. Liu, J. Zang, S. G. E. te Velthuis, A. Hoffmann, *Phys. Rep.* **2017**, *704*, 1.

[6] K. Everschor-Sitte, J. Masell, R. M. Reeve, M. Kläui, *J. Appl. Phys.* **2018**, *124*, 240901.

[7] G. Finocchio, F. Büttner, R. Tomasello, M. Carpentieri, M. Kläui, *J. Phys. D: Appl. Phys.* **2016**, *49*, 423001.

[8] R. Tomasello, E. Martinez, R. Zivieri, L. Torres, M. Carpentieri, G. Finocchio, *Sci. Rep.* **2014**, *4*, 6784.

[9] X. Zhang, M. Ezawa, Y. Zhou, *Sci. Rep.* **2015**, *5*, 9400.

[10] J. Zázvorka, F. Jakobs, D. Heinze, N. Keil, S. Kromin, S. Jaiswal, K. Litzius, G. Jakob, P. Virnau, D. Pinna, K. Everschor-Sitte, L. Rózsa, A. Donges, U. Nowak, M. Kläui, *Nat. Nanotechnol.* **2019**, *14*, 658.

[11] I. Dzyaloshinskii, *J. Phys. Chem. Solids* **1958**, *4*, 241.

[12] T. Moriya, *Phys. Rev.* **1960**, *120*, 91.

[13] W. Jiang, P. Upadhyaya, W. Zhang, G. Yu, M. B. Jungfleisch, F. Y. Fradin, J. E. Pearson, Y. Tserkovnyak, K. L. Wang, O. Heinonen, S. G. E. te Velthuis, A. Hoffmann, *Science* **2015**, *349*, 283.

[14] W. Jiang, X. Zhang, G. Yu, W. Zhang, X. Wang, M. B. Jungfleisch, J. E. Pearson, X. Cheng, O. Heinonen, K. L. Wang, Y. Zhou, A. Hoffman, S. G. E. te Velthhuis, *Nat. Phys.* **2017**, *13*, 162.

[15] K. Litzius, I. Lemesh, B. Krüger, P. Bassirian, L. Caretta, K. Richter, F. Büttner, K. Sato, O. A. Tretiakov, J. Förster, R. M. Reeve, M. Weigand, I. Bykova, H. Stoll, G. Schütz, G. S. D. Beach, M. Kläui, *Nat. Phys.* **2017**, *13*, 170.

[16] K. Litzius, J. Leliaert, P. Bassirian, D. Rodrigues, S. Kromin, I. Lemesh, J. Zázvorka, K.-J. Lee, J. Mulkers, N. Kerber, D. Heinze, N. Keil, R. M. Reeve, M. Weigand, B. V. Waeyenberge, G. Schütz, K. Everschor-Sitte, G. S. D. Beach, M. Kläui, *Nat. Electron.* **2020**, *3*, 30.

[17] S. Woo, K. M. Song, X. Zhang, Y. Zhou, M. Ezawa, X. Liu, S. Finizio, J. Raabe, N. J. Lee, S.-I. Kim, S.-Y. Park, Y. Kim, J.-Y. Kim, D. Lee, O. Lee, J. W. Choi, B.-C. Min, H. C. Koo, J. Chang, *Nat. Commun.* **2018**, *9*, 959.

[18] Y. Hirata, D.-H. Kim, S. K. Kim, D.-K. Lee, S.-H. Oh, D.-Y. Kim, T. Nishimura, T. Okuno, Y. Futakawa, H. Yoshikawa, A. Tsukamoto, Y. Tserkovnyak, Y. Shiota, T. Moriyama, S.-B. Choe, K.-J. Lee, T. Ono, *Nat. Nanotechnol.* **2019**, *14*, 232.

[19] P. Hansen, C. Clausen, G. Much, M. Rosenkranz, K. Witter, *J. Appl. Phys.* **1989**, *66*, 756.

[20] J. Barker, O. A. Tretiakov, *Phys. Rev. Lett.* **2016**, *116*, 147203.

[21] C. D. Stanciu, F. Hansteen, A. V. Kimel, A. Kirilyuk, A. Tsukamoto, A. Itoh, Th. Rasing, *Phys. Rev. Lett.* **2007**, *99*, 047601.

[22] M. S. El Hadri, P. Pirro, C.-H. Lambert, S. Petit-Watelot, Y. Quessab, M. Hehn, F. Montaigne, G. Malinowski, S. Mangin, *Phys. Rev. B* **2016**, *94*, 064412.

[23] Y. Xu, M. Hehn, W. Zhao, X. Lin, G. Malinowski, S. Mangin, *Phys. Rev. B* **2019**, *100*, 064424.

[24] Y. Xu, M. Deb, G. Malinowski, M. Hehn, W. Zhao, S. Mangin, *Adv. Mater.* **2017**, *29*, 1703474.

[25] M. Weißenhofer, U. Nowak, *New J. Phys.* **2020**, *22*, 103059.

[26] M. R. Scheinfein, J. Unguris, M. H. Kelley, D. T. Pierce, R. J. Celotta, *Rev. Sci. Instrum.* **1990**, *61*, 2501.

[27] P. Krautscheid, R. M. Reeve, M. Lauf, B. Krüger, M. Kläui, *J. Phys. D: Appl. Phys.* **2016**, *49*, 425004.

[28] D. Schönke, A. Oelsner, P. Krautscheid, R. M. Reeve, M. Kläui, *Rev. Sci. Instrum.* **2018**, *89*, 083703.

[29] E. C. Corredor, S. Kuhrau, F. Kloodt-Twesten, R. Frömter, H. P. Oepen, *Phys. Rev. B* **2017**, *96*, 060410(R).

[30] F. Kloodt-Twesten, S. Kuhrau, H. P. Oepen, R. Frömter, *Phys. Rev. B* **2019**, *100*, 100402(R).

[31] B. A. Lilley, *Philos. Mag.* **1950**, *41*, 792

[32] R. Lavrijsen, D. M. F. Hartmann, A. van den Brink, Y. Yin, B. Barcones, R. A. Duine, M. A. Verheijen, H. J. M. Swagten, B. Koopmans, *Phys. Rev. B* **2015**, *91*, 104414.

[33] N. Papanicolaou, *Solitons*, Springer, New York, NY **2000**, p. 167.

[34] B. Göbel, A. F. Schäffer, J. Berakdar, I. Mertig, S. S. P. Parkin, *Sci. Rep.* **2019**, *9*, 12119.

[35] F. Büttner, C. Moutafis, M. Schneider, B. Krüger, C. M. Günther, J. Geilhufe, C. v. Korff Schmising, J. Mohanty, B. Pfau, S. Schaffert, A. Bisig, M. Foerster, T. Schultz, C. A. F. Vaz, J. H. Franken, H. J. M. Swagten, M. Kläui, S. Eisebitt, *Nat. Phys.* **2015**, *11*, 225.

[36] X. Zhang, J. Xia, Y. Zhou, D. Wang, X. Liu, W. Zhao, M. Ezawa, *Phys. Rev. B* **2016**, *94*, 094420.

[37] I. Lemesh, F. Büttner, G. S. D. Beach, *Phys. Rev. B* **2017**, *95*, 174423.

[38] U. Atxitia, D. Hinzke, O. Chubykalo-Fesenko, U. Nowak, H. Kachkachi, O. N. Mryasov, R. F. Evans, R. W. Chantrell, *Phys. Rev. B* **2010**, *82*, 134440.

[39] L. Rózsa, U. Atxitia, U. Nowak, *Phys. Rev. B* **2017**, *96*, 094436.

[40] T. Nakamura, M. Bloch, *Phys. Rev.* **1963**, *132*, 2528.

[41] C. M. Srivastava, R. Aiyar, *J. Phys. C: Solid State Phys.* **1987**, *20*, 1119.

[42] N. Bergeard, T. Ferté, C. Boeglin, F. Radu, R. Abrudan, T. Kachel, unpublished.

[43] A. Belabbes, G. Bihlmayer, F. Bechstedt, S. Blügel, A. Manchon, *Phys. Rev. Lett.* **2016**, *117*, 247202.

[44] S. Heinze, K. von Bergmann, M. Menzel, J. Brede, A. Kubetzka, R. Wiesendanger, G. Bihlmayer, S. Blügel, *Nat. Phys.* **2011**, *7*, 713.

[45] H. Yang, A. Thiaville, S. Rohart, A. Fert, M. Chshiev, *Phys. Rev. Lett.* **2015**, *115*, 267210.

[46] R. Frömter, S. Hankemeier, H. P. Oepen, J. Kirschner, *Rev. Sci. Instrum.* **2011**, *82*, 033704.

[47] S. Kuhrau, F. Kloodt-Twesten, C. Heyn, H. P. Oepen, R. Frömter, *Appl. Phys. Lett.* **2018**, *113*, 172403.

[48] H. P. Oepen, R. Frömter, *Handbook of Magnetism and Advanced Magnetic Materials*, Wiley, Hoboken, NJ **2007**, p. 1442.